Red-Emitting Manganese-doped Aluminum Nitride Phosphor

Nerine J. Cherepy, Stephen A. Payne, Nicholas M. Harvey, Daniel Åberg, Zachary M. Seeley, Kiel S. Holliday, Ich C. Tran, Fei Zhou, H. Paul Martinez, Jessica M. Demeyer, Alexander D. Drobshoff
Lawrence Livermore National Laboratory, Livermore, CA 94550

Alok M. Srivastava, Samuel J. Camardello, Holly A. Comanzo
GE Global Research, One Research Circle, Niskayuna, NY 12309

Deborah L. Schlagel, Thomas A. Lograsso
Ames National Laboratory, Ames, IA 50011

Abstract

We report high efficiency luminescence with a manganese-doped aluminum nitride red-emitting phosphor under 254 nm excitation, as well as its excellent lumen maintenance in fluorescent lamp conditions, making it a candidate replacement for the widely deployed europium-doped yttria red phosphor. Solid-state reaction of aluminum nitride powders with manganese metal at 1900 °C, 10 atm N_2 in a reducing environment results in nitrogen deficiency, as revealed by EDS and diffuse reflectance spectra. When these powders are subsequently annealed in flowing nitrogen at 1650 °C, higher nitrogen content is recovered, resulting in white powders. Silicon was added to samples as an oxygen getter to improve emission efficiency. NEXAFS spectra and DFT calculations indicate that the Mn dopant is divalent. From DFT calculations, the UV absorption band is proposed to be due to an aluminum vacancy coupled with oxygen impurity dopants $(V_{Al}\text{-}2O_N)^-$, and Mn^{2+} is assumed to be closely associated with this site. In contrast with some previous reports, we find that the highest photoluminescence efficiency (Q.E. = 0.86±0.14) is obtained in aluminum nitride with a low manganese doping level of 0.06 mol%. The principal Mn^{2+} decay of 1.25 ms is assigned to non-interacting Mn sites, while additional components in the microsecond range appear with higher Mn doping, consistent with Mn clustering and resultant exchange coupling. Slower components are present in samples with low Mn doping, as well as strong afterglow, assigned to trapping and de-trapping on shallow traps.

Keywords: Red phosphor; aluminum nitride; manganese emission

*Corresponding author.
E-mail address: cherepy1@llnl.gov
Telephone: 925-424-3492
FAX: 925-423-6394

Introduction

Nitride phosphors have taken on significance in recent years, particularly for solid-state lighting [1]. Among the red-emitting nitride phosphors reported, most are activated with Eu^{2+}, providing absorption of blue LED excitation and broad emission bands extending beyond 750 nm. Most nitrides offer luminescence without activation, some emitting in the red [2] and some red-emitting Mn^{2+} doped nitrides have been studied [3,4]. Red luminescence in aluminum nitride (AlN) doped with Mn has been reported in numerous publications since the 1960's [5,6], and while the emission was originally interpreted as deriving from Mn^{4+} [7,8], more recently it has been interpreted as Mn^{2+} [9]. Mn^{2+}-activated phosphors have been used extensively in fluorescent lighting. In early years, the natural Willemite mineral, $(Zn,Be)_2SiO_4:Mn^{2+}$, was employed, and later the Sb^{3+},Mn^{2+}- doped halophosphates [10].

Aluminum nitride is widely used as a substrate for circuitry and semiconductor devices, owing to its excellent thermal conductivity and compatibility with other nitrides. Synthesis of AlN powder used for sintered AlN ceramics is performed industrially through a variety of synthetic pathways, including carbothermal reduction nitridation [11], gas-reduction nitridation of powders or aerosols [11,12], and metal-organic routes [13]. We demonstrate here a simple, scalable approach for low-cost manufacture, employing solid-state reaction of pure hexagonal wurtzite AlN powders with Mn dopant.

To obtain the highest light yields in Mn^{2+}-doped phosphors, Mn clustering must be avoided, as it results in quenching of emission, described as early as 1963 by McClure in ZnS, and in other hosts, such as $MgAl_2O_4$ and $ZnGa_2O_4$ [14-16]. The optimal Mn concentration in AlN has been studied in thin films, and found to be 3-8x10^{19} cm^3 (0.03-0.08 at%) by Sato [7,8], though several recent papers have surprisingly reported optimal doping concentrations of 1-3% [9,17].

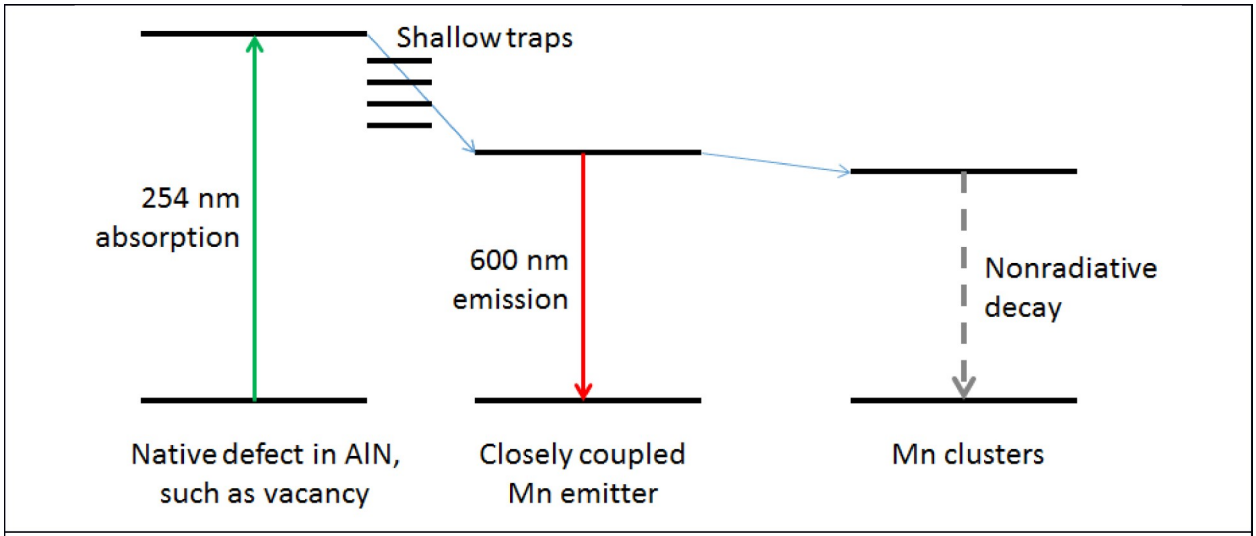

Figure 1. Energy level diagram for functionality of the AlN:Mn phosphor in a fluorescent lamp.

The origin of the near-UV absorption band at 4.5-5 eV, observed for undoped AlN (band gap 6.2 eV), has been assigned by Trinkler and others to radiative recombination of two proximal oxygen-related defects forming a donor-acceptor pair: O_N-v_{Al} (an oxygen ion substituting for nitrogen O_N and aluminum vacancy v_{Al} nearby), the excited state of which may ionize to populate the conduction band [18-20]. Subsequently, AlN intrinsic luminescence is thought to derive from trapping of this excitation on another O_N. A simplified energy level diagram, shown in Figure 1, describes the luminescence mechanism for AlN:Mn. For Mn-doped AlN, the intrinsic luminescence of AlN is a minor pathway, and therefore is not shown, instead, the excited state of Mn^{2+} is populated directly from the conduction band, or indirectly after trapping on shallow defects. The strong afterglow reported previously for both undoped [18] and doped AlN phosphors [17] is consistent with the UV absorption populating the conduction band of AlN, and the subsequent delayed luminescence resulting from the presence of shallow traps (likely nitrogen vacancies). Other recent studies have found that AlN:Mn is an excellent cathodoluminescent phosphor [9], and reported emission efficiency of ~80% with 320 nm excitation [21]. There are no prior published studies of the use of AlN phosphors in a mercury discharge lamp, which is the focus of this paper.

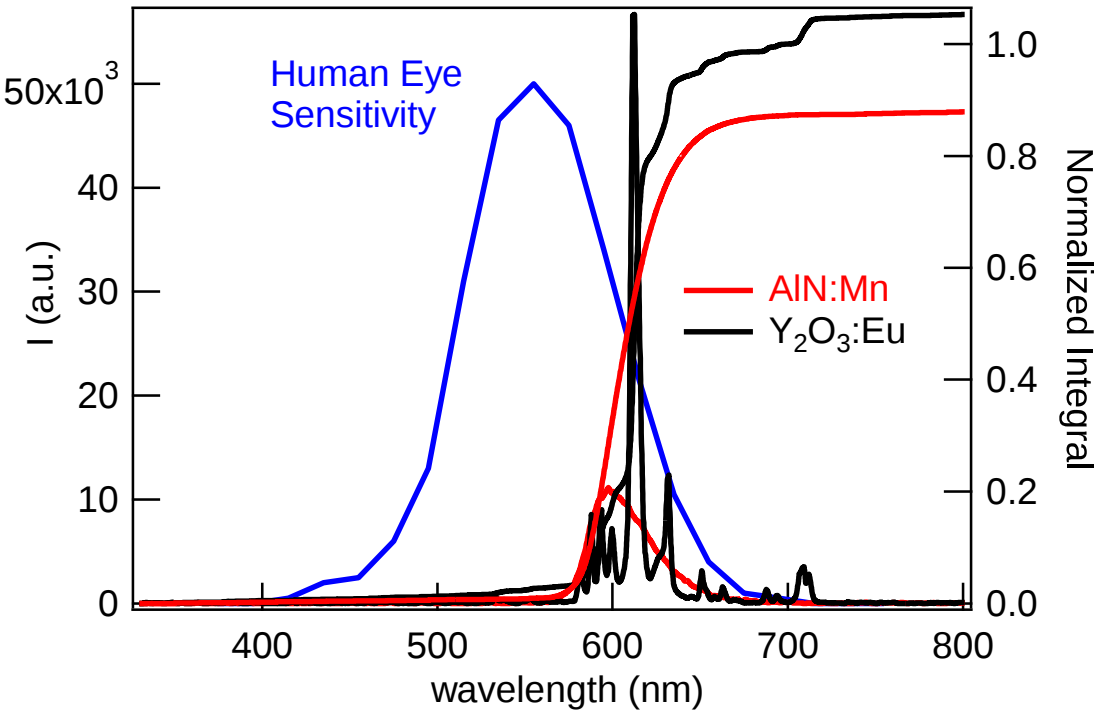

Figure 2. Emission spectra excited at 254 nm of AlN:Mn and Y_2O_3:Eu (solid lines), data acquired with identical geometry and slit widths and thus the spectra may be compared quantitatively. The integrated intensities of the spectra, normalized to the value at 700 nm for Y_2O_3:Eu (short dashed lines) show that under these conditions the (A_{254} x Q.E.) product for AlN:Mn is >80% that of Y_2O_3:Eu. Also shown is the human eye sensitivity curve (long dashed line).

Requirements for fluorescent lamp phosphors include high efficiency luminescence under 254 nm Hg line excitation and minimal reaction with mercury or degradation by UV [22]. These requirements eliminate many candidate phosphors. Furthermore, a useful red phosphor must emit only in the narrow spectral range of 590-650 nm (C.I.E. coordinates of x = 0.62-0.66 and y = 0.33-0.38), most preferably near 615 nm, where the balance between lumen efficiency (human eye sensitivity) and color rendition is optimal. Figure 2 shows that the emission spectra of AlN:Mn and Y_2O_3:Eu are remarkably well-matched, with CIE coordinates (x = 0.620, y = 0.379) and (x = 0.644, y = 0.354) respectively; slightly more yellow emission is present in the AlN:Mn spectrum, resulting in higher lumen efficiency, while the emission band in Y_2O_3:Eu beyond 700 nm is off the eye sensitivity curve. The product of the absorbance at 254 nm (A_{254}) and the quantum efficiency (Q.E.) measured for the best AlN:Mn phosphors We report here for the first time that the red AlN:Mn phosphor meets the requirements for implementation in fluorescent lamps, including emission color, high efficiency, and survival in mercury discharge.

Experimental

Synthesis. Commercial aluminum nitride powders (Materion or H.C. Starck; materials used here are nominally 33.3% N, 0.1% C, <1% O, <0.005% Fe, with surface area of 2 m^2/g) were ground with Mn and Si dopants (Sigma Aldrich) in an agate mortar, placed in boron nitride crucibles, and heated under 10-100 atm nitrogen pressure at 1900 °C for 4 hours. Specimens prepared in this way had grayish-white body color. Powders were then ground again, and annealed in flowing nitrogen at 1650 °C, after which the body color became white. Mn concentration was determined by GDMS (Northern Analytical), and cross-correlated with the intensity of the 520 nm Mn excitation peak for ongoing assessment of Mn concentration of samples.

Structure.

Near-Edge X-ray Absorption Fine Structure

Near edge x-ray absorption fine structure (NEXAFS) measurements were performed at the beamline 8.2 of the Stanford Synchrotron Radiation Lightsource (SSRL, SPEARIII) at the Stanford Linear Accelerator Center (SLAC). The cross-section of the focused beam was approximately 1 mm in diameter at normal to the sample surface. Samples in fine powder form were spread into thin films on double-sided adhesive, conductive carbon tape attached to the sample holder. Experiments were performed at room temperature and with the linear polarized incident beam normal to sample surfaces. NEXAFS spectra at Mn *L*-edge were collected in surface-sensitive total electron yield (TEY) mode. All the spectra have been normalized to the beam flux, which was recorded via a Au grid located upstream of the experimental sample. The experimental energy resolution is better than 0.15 eV.

X-ray Diffraction

Powder x-ray diffraction (XRD) was performed with a Bruker D8 Advanced diffractometer equipped with a Cu anode ($K\alpha_1$ = 0.1540598 nm). Samples were prepared by spreading the powder on a low-background sample holder (single crystal silicon wafer) with the aid of methanol. Patterns were taken using 40 mV and 40 mA from 10 to 90° 2θ with a step size of 0.015° 2θ and 1.5 s per step. Phases were identified using Bruker AXS EVA.

Electron Microscopy

Electron microscopy was performed on a FEI Inspect F scanning electron microscope. Micrographs were collected in both secondary electron and backscattered electron mode using an accelerating voltage of 15 kV, working distance of 11.5 mm, and a spot size of 5.5 units. Samples were prepared by dispersing the powder onto conductive carbon tape. Energy dispersive spectroscopy was performed with a Bruker Quantax detector.

Spectroscopy.

At LLNL, phosphor samples were mixed 50/50 vol% with a fluoropolymer in acetone and dispersed ultrasonically, forming non-friable easily handled opaque films via sedimentation, in which the higher density phosphor powder settles to the bottom of the film, for optical characterization in which the optical contribution of the fluoropolymer binder is negligible. Reflectance spectra were acquired at LLNL with a Perkin Elmer Lambda 19 and measured against a $BaSO_4$ standard. A Thermo Lumina luminescence spectrometer was used at LLNL to acquire emission spectra of phosphor samples in reflectance mode, referencing to a standard Y_2O_3:Eu phosphor from GE acquired with identical excitation conditions and geometry, and integrated intensities compared to determine relative light yields. Lifetime measurements were acquired using a flashlamp-pumped Nd:YAG laser at 266 nm with 20 ns pulses. Luminescence was collected with a monochromator, set to the emission wavelength, coupled to an R928 Hamamatsu PMT and read out by an oscilloscope. For each measurement, 25 traces were acquired and averaged to generate the decay curves, which were then fit in Igor Pro to obtain the decay components and their amplitudes.

Quantum Simulations.

Calculations were performed within density functional theory (DFT) using the projector augmented wave (PAW) method [23] as implemented in the Vienna Ab initio Simulation Package [24,25]. For the bulk of the calculations, exchange-correlation (XC) effects were treated within the generalized gradient spin approximation [26]. Absorption energies were calculated using the more accurate PBE0 hybrid energy functional [27] and imposing constraints on the spin density. The plane wave energy cutoff was set to 520 eV and Gaussian smearing with a width of 0.1 eV was used to determine occupation numbers. The bulk of the computational data presented in the following were obtained using 240 atom supercells together with a Γ-point sampling of the Brillouin zone. Configurations were relaxed until ionic forces were less than 20 meV/Å. Point defect formation energies for charge state *q* were calculated as outlined in [28-30] according to

$$\Delta E_f = E_{¿} - E_{id} + q\left(\varepsilon_{VBM} + \mu_e\right) - \sum_i^{\square} \Delta n_i \mu_i ,$$

where $E_{¿}$ is the total energy of the system containing the defect and E_{id} is the total energy of the ideal host. The second term describes the dependence on the electron chemical potential, μ_e, which is measured with respect to the valence band maximum (VBM), ε_{VBM}

. The formation energy also depends on the chemical potentials of the constituents as given by the last term, where the difference between the number of atoms of type *i* in the ideal cell with respect to the defect cell is denoted by Δn_i. The spurious image charge interaction is taken into account via the standard Makov-Payne correction [31].

Quantum efficiency measurement and mercury lamp testing.

The quantum efficiency of the phosphor, which is defined as the ratio of the number of photons emitted by the phosphor sample to the number of ultraviolet photons absorbed, was determined at GE by measuring the ultraviolet reflectance of the sample and the standard phosphor (Y_2O_3:Eu^{3+}; GE Lighting) relative to $BaSO_4$ and by measuring the integrated intensity of the sample relative to standard phosphor. A reflectance value of 0.952 for $BaSO_4$ illuminated with 254 nm light was used to determine the reflectance values. Exposure to mercury vapor and plasma conditions were studied using the GE proprietary "racetrack" lamp system (electrodeless fluorescent lamp) that is an accelerated testing apparatus. Commercial lighting phosphors exhibited very little brightness loss (-1.6%±1.6%) when exposed to the discharge in the racetrack apparatus whereas phosphors such as Zn_2SiO_4:Mn that are known to be mercury unstable exhibited brightness loss of (-14% ±4.1%) within the first hour of exposure. Although prolonged testing in a fluorescent lamp is the final indicator for the long term lumen maintenance of any new phosphor, the racetrack lamp system provides a rapid screening tool for determining the compatibility of the new phosphor with the mercury/rare earth discharge.

Results and Discussion

Mn valence in AlN host.

The ionic radii of both Al^{3+} and Mn^{4+} in tetrahedral coordination is 39 pm, while that of Mn^{2+} is 66 pm, and primarily due to the expectation of ionic radius matching, many papers historically assigned the Mn-related emission in the 560-670 nm range to Mn^{4+}. Mn^{2+} is large for the Al^{3+} site, as well as aliovalent, inviting hypotheses that Mn^{2+} may substitute proximally with an O^{2-} substitution for nitrogen, for charge balance [18]. NEXAFS data are shown in Figure 3A of a typical AlN:Mn sample, along with MnO_2 and $MnCO_3$ reference samples, representing Mn^{4+} and Mn^{2+} standards, respectively. The AlN:Mn absorption closely resembles the Mn^{2+} standard [32,33], while no evidence of Mn^{4+}, is observed, contrary to earlier studies which surmised Mn^{4+} to be more stable in AlN [6,8].

Figure 3B displays thermodynamic formation energies for substitutional and interstitial Mn. It can be seen that Mn substitutes for Al in the 2+ charge state (q = -1) for both Al and N-rich conditions for electron chemical potentials (Fermi levels) above 2 eV. The same conclusion holds for calculations using smaller 96-atom cells with the more accurate PBE0 energy functional (not shown).

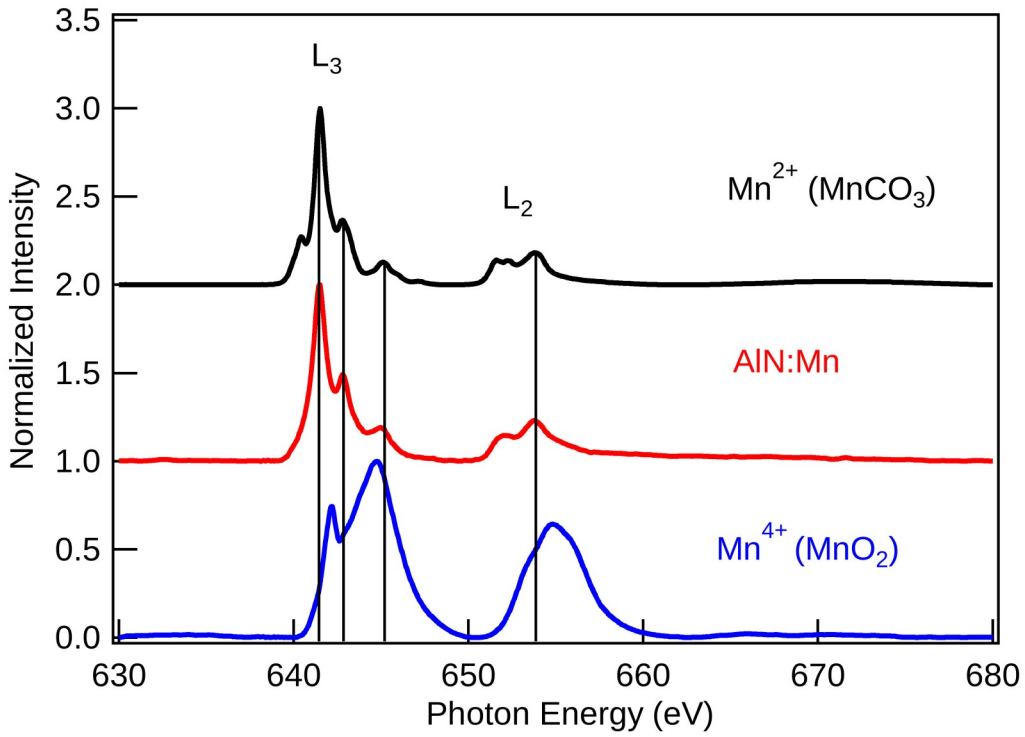

Figure 3A. NEXAFS spectra of a typical AlN:Mn sample shows a good match with the Mn^{2+} standard.

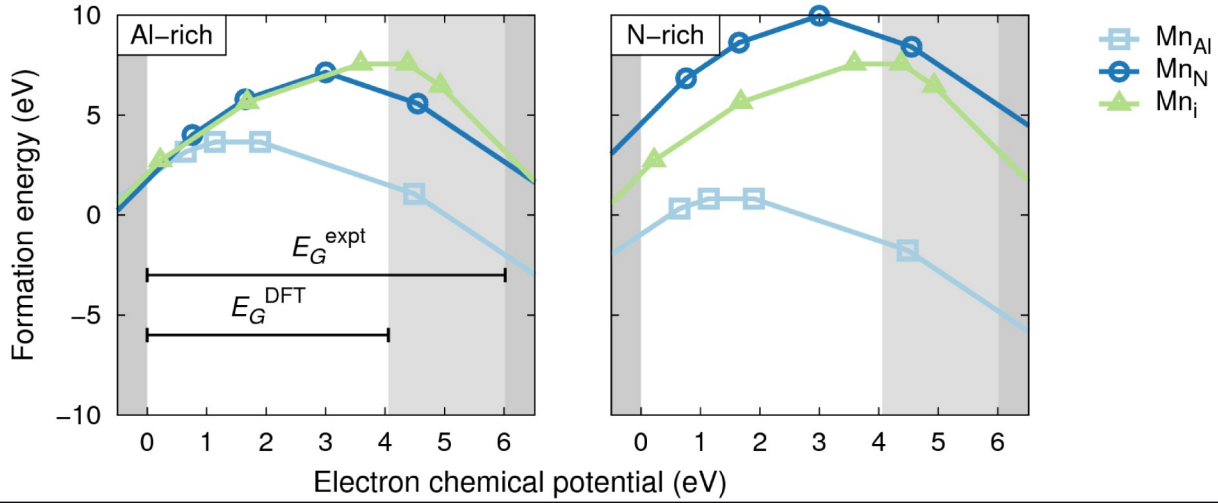

Figure 3B. Formation energies of substitutional and interstitial Mn in AlN as a function of the electron chemical potential (Fermi level) for Al-rich **(left)** and N-rich **(right)** conditions. The slope of the line corresponds to the charge state (only the charge state with lowest formation energy is shown), The white region indicates the calculated band gap while the lighter gray region indicates the difference between the experimental and the calculated band gap. These calculations show that Mn substituting on Al with the 2+ charge state is most stable.

Structure and Particle Size.

As-received powders formed by direct nitridation are somewhat porous, with ≈1 micron size primary particles and average agglomerate size of ≈10 microns, as shown in Figures 4A and 4B. After firing with Mn and Si dopants at 1900°C and 10 atm N_2 pressure, followed by annealing at 1650°C in flowing nitrogen the particles appear more crystalline, with primary particles ≈5 microns in size, and sintering to larger agglomerates of 10-30 microns occurs (Figures 4C and 4D).

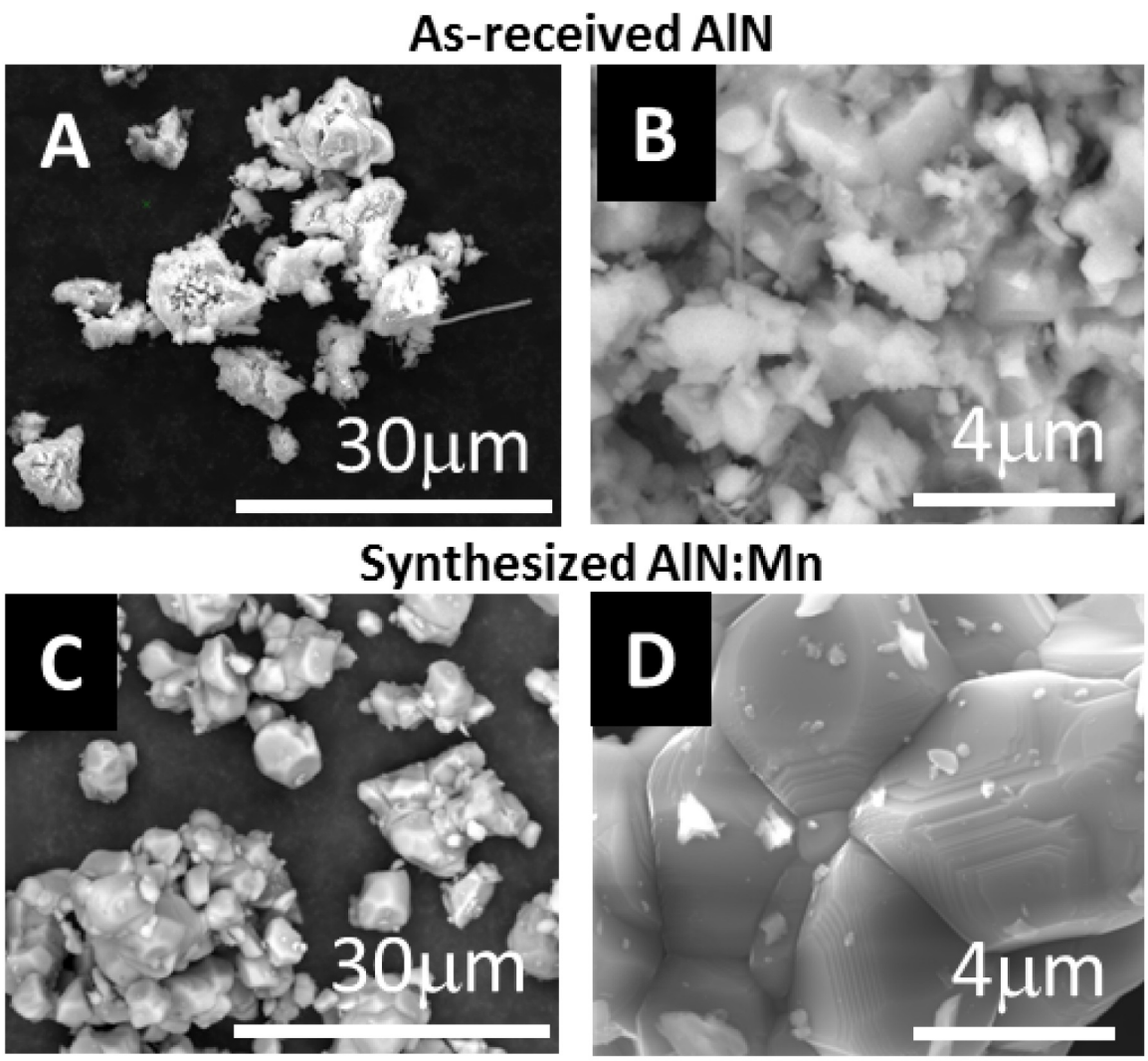

Figure 4. (A) and **(B)** As-received powders show porosity and <10 μm primary particles, **(C)** after doping at 1900°C and annealing 1650°C better crystallinity is achieved. **(D)** At higher magnification, faceting and hexagonal steps are visible on particle surfaces.

Nitrogen Annealing.

After the initial firing at 1900°C, the phosphor body color is grayish white, indicative of non-stoichiometry and nitrogen vacancies. Nitrogen vacancies have been attributed previously to a broad absorption in the visible wavelengths in single crystal AlN (vicinity of 450 nm) [19,34]. Although AlN is thought to sublime congruently, its vapor pressure is about 100x higher at 1900°C than at 1650°C [35]. Furthermore, we perform the synthesis in a graphite furnace, and the highly reducing atmosphere may enhance nitrogen deficiency in the material. When the as-synthesized powders are subsequently treated at 1650°C in flowing nitrogen, we find that they become significantly whiter. The diffuse reflectance spectrum of an AlN:Mn sample before and after subsequent annealing are shown in Figure 5. Improved luminescence efficiency upon annealing is shown in the photo in Figure 5 of the phosphor samples under 254 nm excitation; the bottom sample (after annealing) is brighter than the middle one (before annealing). Measured emission efficiency improves by at least 20% for all samples after nitrogen annealing, while neither the absorption at 254 nm nor that at 600 nm changes significantly. This is likely due to removal of defects that serve as deep traps, as well as elimination of parasitic optical absorption. We performed SEM/EDS measurements of grayish samples and found the Al/N ratio to be higher than for whiter samples, additionally confirming our hypothesis that the dark color derives from nitrogen vacancies (see Supplementary Information). We hypothesize that a subnitride formed at 1900°C and is converted back to the stoichiometric (or near-stoichiometric) composition in flowing nitrogen at 1650°C.

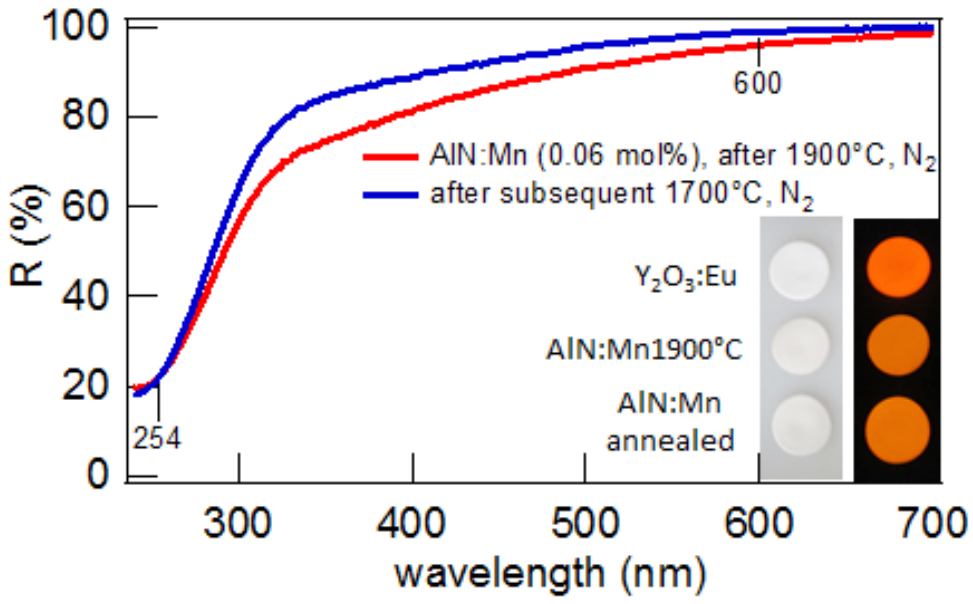

Figure 5. The diffuse reflectance of AlN:Mn after synthesis at 1900°C and 10 atm N_2 shows evidence of a broad absorption throughout the visible. Improved reflectance is obtained after AlN:Mn samples are annealed in flowing nitrogen at 1650°C. **(inset)** The photos show the body color of AlN:Mn before and after annealing, in comparison with the standard red phosphor, Y_2O_3:Eu. Improved luminescence is apparent in the photo at right, of the same samples under 254 nm excitation.

X-Ray diffraction patterns of samples reveal the well-known AlN hexagonal wurtzite phase, with less than 1% of secondary phase contributions to any pattern (Figure 6). Patterns acquired before and after nitrogen annealing appear unchanged, and cannot be used to support or refute hypotheses regarding the role of the nitrogen anneal step in improving luminescence efficiency or phosphor body color. (see Supplementary Information).

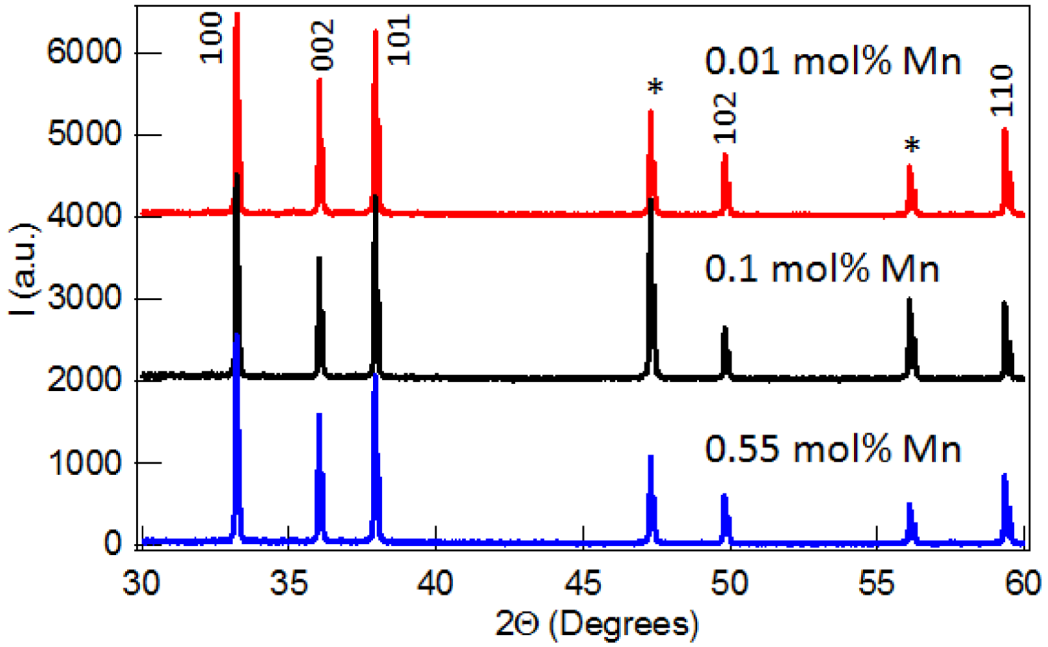

Figure 6. X-ray diffraction patterns of several AlN:Mn samples after annealing. All are pure phase hexagonal wurtzite structure. The peaks marked with (*) are due to the Si internal calibration standard.

Luminescence Mechanism.

Prior reports of UV absorption features in single crystal AlN have been assigned to oxygen defects (222-313 nm) [19], while samples with very low oxygen content exhibit band-edge emission at ≈200nm. Higher oxygen content is correlated with oxygen defect-associated emission in the ≈400 nm range [20]. While most models of the UV optical absorption of AlN have postulated that this transition due to an absorption from the ground state to the excited state of an O_N-v_{Al} complex, the excited state lying near or in the conduction band of AlN, and the subsequent ~400 nm emission occurring from a higher-lying O_N level, not associated with a v_{Al} [18, 9]. This model is based on the existence of an O_N-associated level in the middle of the gap. To this end, we display in Figure 7A (Al-rich stoichiometry) and 7B (N-rich stoichiometry) the formation energies of the intrinsic defects and oxygen impurities and complexes. As has been well established in the literature [36-38], the dominant intrinsic defects

in AlN are the aluminum (acceptor in charge state +3) and nitrogen(donor in charge state -1) vacancies. Furthermore, our DFT calculations, as well as others [39], show that oxygen preferentially substitutes on a nitrogen site as a shallow +1 donor. As can be seen in Fig. 7C, O_N has no deep transition levels in the gap and can hence not explain the 400 nm emission. Due to their opposing charges, we find in accordance with Ref. [39] that O_N can form stable complexes with an aluminum vacancy. In fact, as displayed in Fig. 7D, the nearest-neighbor complexes formed from a v_{Al} and one, two, or three O_N are all stable. Since the ground states of these complexes are predominantly spin-compensated (S=0) across the available electron chemical potential, we calculate their excited state by imposing the approximate constraint S=2. The resulting absorption energies along with the theoretical results of Yan et al. [39] are displayed in Table 1. The latter values were calculated using ground state energies assuming transitions to an empty conduction band. Nevertheless, the agreement is fair, indicating that the Al vacancy and its complexes with oxygens can give rise to the observed absorption of about 280 nm, as observed in the excitation spectra for the intrinsic emission from undoped AlN. We do not speculate further on the 400 nm emission observed in Mn-free samples but again emphasize that the O_N impurity probably plays no role in this emission.

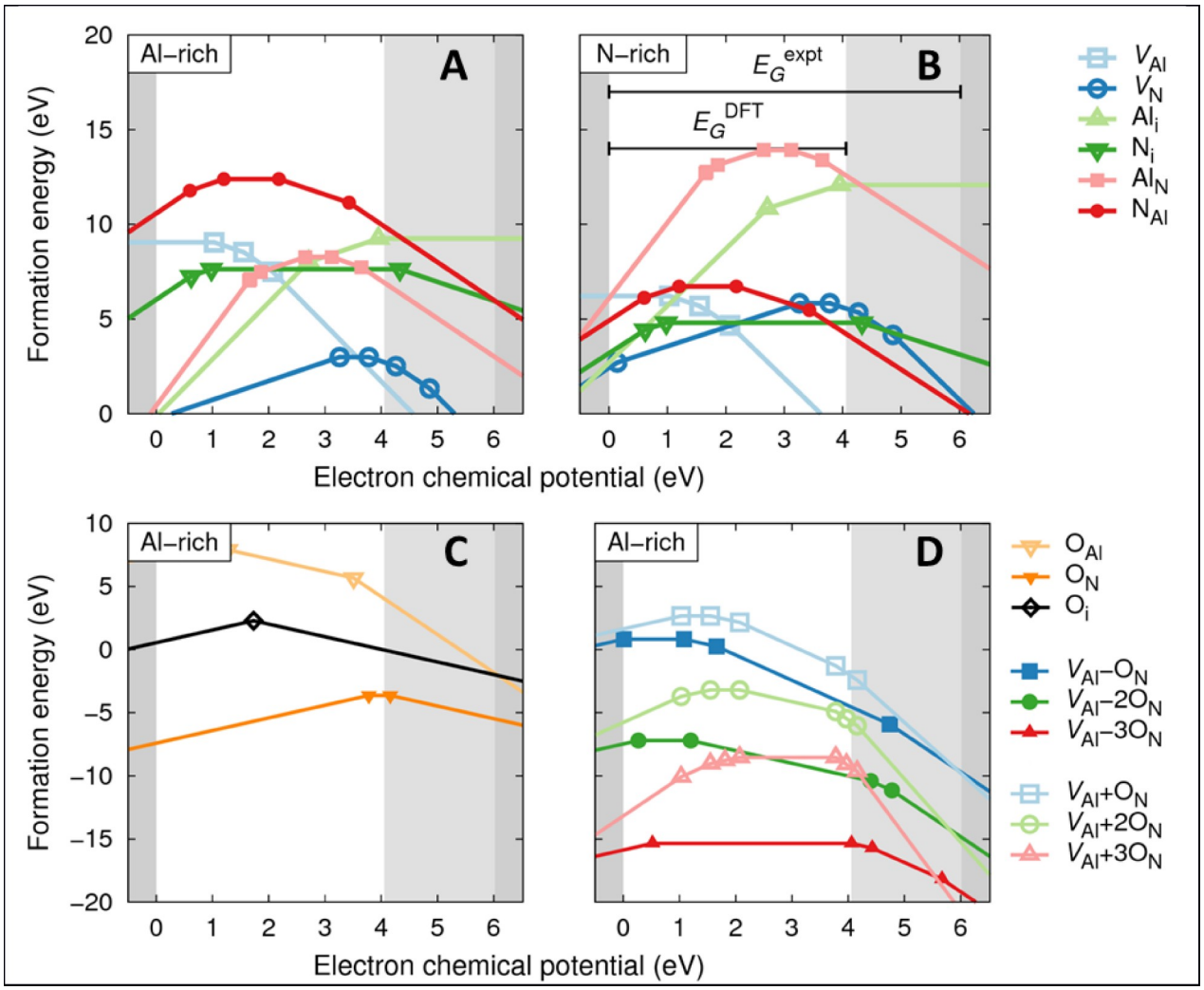

Figure 7. (A) and **(B)** Formation energies of intrinsic defects under Al and N-rich conditions. **(C)** Formation energies of oxygen impurities under Al-rich conditions as a function of electron chemical potential. **(D)** Formation energies of a variety of possible complexes. X-Y implies a nearest neighbor complex formed from defects X and Y, whereas X+Y denotes the sum of the isolated individual formation energies of the constituents. Thus, we see that all aluminum vacancy-oxygen complexes considered here bind.

Table 1: Calculated absorption energies by intrinsic defects and oxygen impurities.

Defect/impurity	GGA (nm)	PBE0 (nm)	Yan *et al.* [39] (nm)
V_{Al}^{3-}	419	310	-
V_N^{+}	385	366	-
$(V_{Al}\text{-}O_N)^{2-}$	407	310	312
$(V_{Al}\text{-}2O_N)^{-}$	384	308	288
$(V_{Al}\text{-}3O_N)^{0}$	340	285	-

A recent study of Si doping of AlN proposed that Si acts as a getter for oxygen, volatilizing away at high temperature as SiO. The ideal Si addition should serve to reduce oxygen content of the AlN starting material, but perhaps not completely remove all oxygen. Excessive Si addition has been shown to decrease the cathodoluminescence efficiency of the intrinsic AlN emission [40,41]. All of the samples synthesized here employed 0.5-1% Si as an oxygen scavenger, which is thought to volatilize away, taking oxygen with it, during the 1900°C synthesis, as evidenced by our observation of Si_3N_4 deposition on the exterior of the boron nitride crucibles upon cooldown in the nitrogen furnace (data not shown). Samples synthesized without silicon, but all other constituents remaining the same, offer about 25% lower efficiency. In our studies of undoped AlN, the intrinsic (defect-related) emission at ~400 nm increases with 0.5-1% Si co-doping, but decreases at higher Si concentrations (see Supplementary Information). An additional possible effect of the presence of Si^{4+} as a co-dopant involves it acting as a charge compensator, possibly stabilizing Al vacancy sites [42].

Mn Concentration Series.

In order to explore the effect of Mn concentration on emission efficiency, a series of samples were synthesized at 1900°C, followed by annealing at 1650°C in flowing nitrogen. The five samples with Mn concentration ranging from 0.01-0.55 mol% are shown in Figure 8; body color under room lights is comparable to that of Y_2O_3:Eu. Under UV excitation, poorer emission efficiency is observed with too low Mn concentration (0.01%) and too high (0.29 and 0.55%), while the 0.06-0.1%Mn samples are comparable to Y_2O_3:Eu. Figure 9 shows the excitation and emission spectra of the five samples. In addition to the strong UV absorption band at ~280 nm, several weak spin and parity forbidden d-d excitation bands can be seen in the highly doped samples, from the $^6A_1(^6S)$ ground state to the excited states: $^4E(^4D)$, at 399 nm, $^4T_2(^4D)$, at 455 nm, $^4A_1(^4G)$, $^4E(^4G)$] at 488 nm, $^4T_2(^4G)$ at 520 nm, and $^4T_1(^4G)$ at 548 nm [Wang]. The inset shows

normalized emission spectra for the 0.01, 0.1 and 0.55 mol% Mn samples. While the spectra from the 0.01 and 0.1 mol% Mn samples are identical, an additional lower energy emission band is present in the 0.55 mol% Mn sample, similar to observations in other nitride phosphors with high Mn doping [3]. Figure 10 shows the dependence of the luminescence efficiency on Mn doping. Quantum efficiency of 0.86±0.14 is achieved at 0.06 mol% Mn. The UV excitation band maximum is found to shift to the red as a function of Mn doping, also shown in Figure 9.

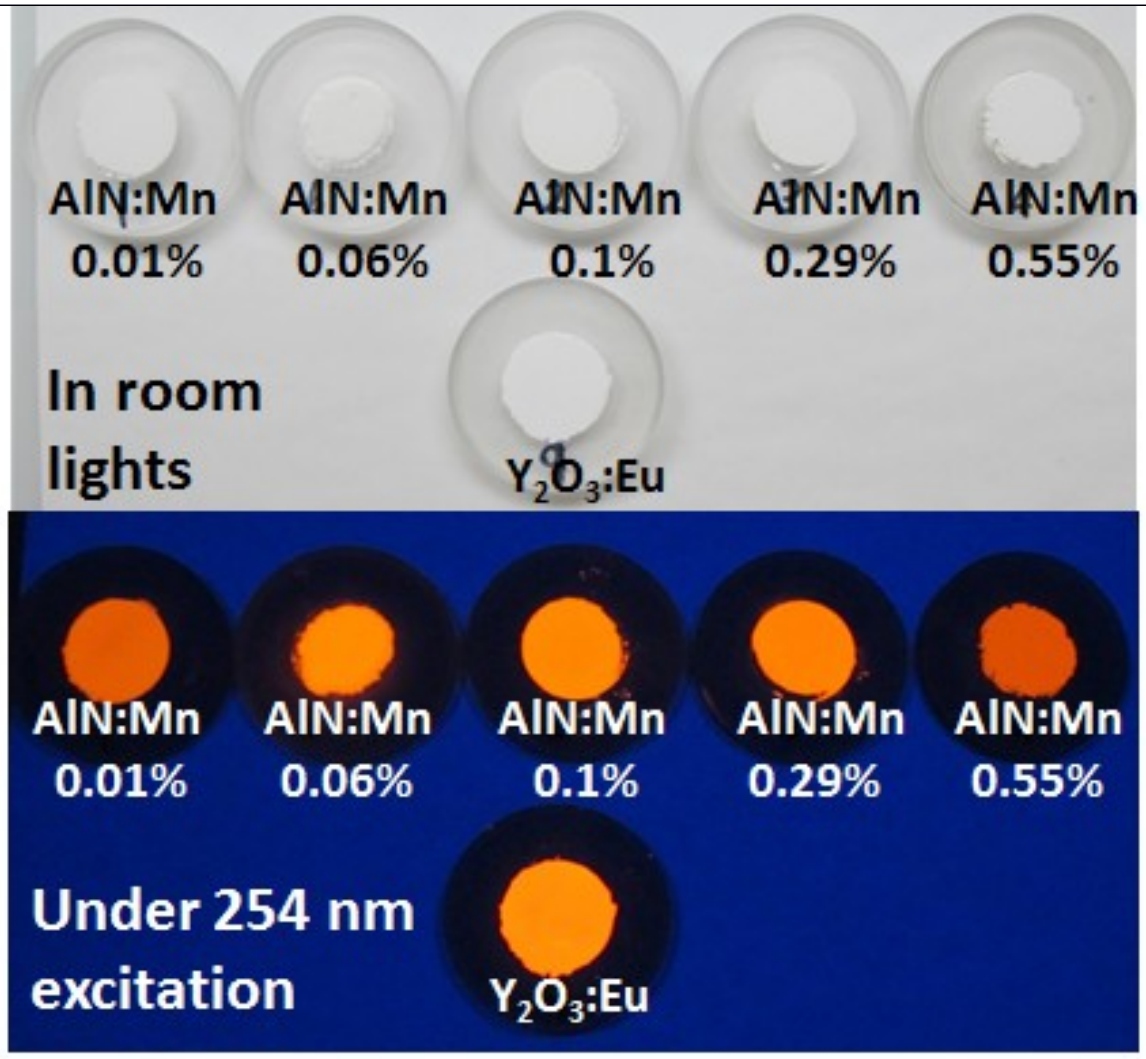

Figure 8. Mn doping concentration series, powders shown after synthesis and annealing, compared to Y_2O_3:Eu, **(top)** under room lights illumination, and **(bottom)** under short-wave Mercury lamp illumination. Poorer emission is observed with too low Mn concentration (0.01%) and too high (0.29 and 0.55%), while the 0.06-0.1%Mn samples are comparable to Y_2O_3:Eu in brightness under UV excitation.

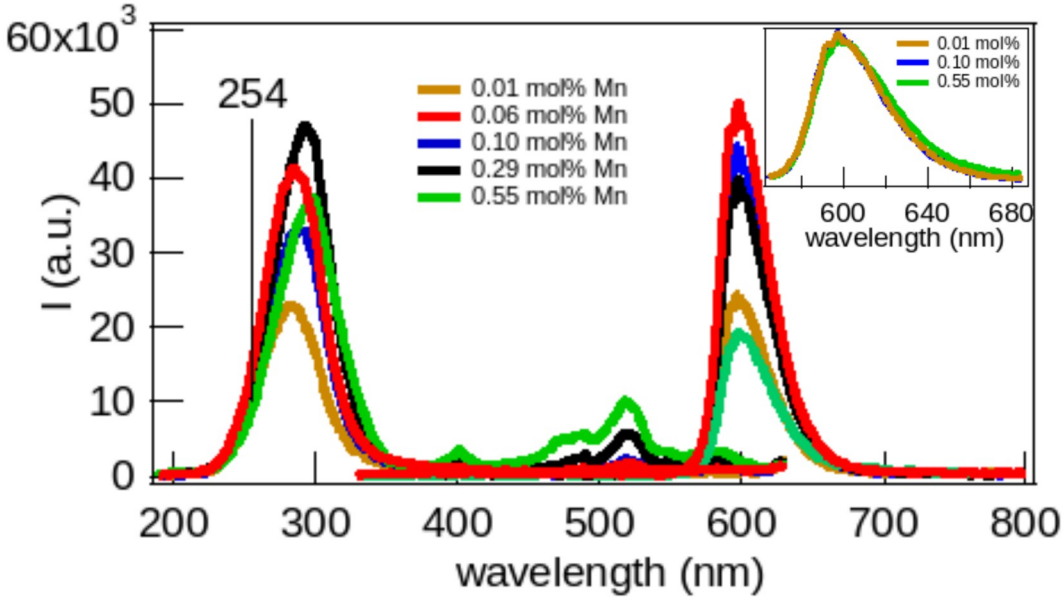

Figure 9. Excitation spectra (emission at 640 nm) and emission spectra (excitation at 254 nm) for a series of AlN:Mn phosphors with varying Mn concentrations. The UV excitation band shifts to the red and the Mn^{2+} absorption features in the visible region become more pronounced as a function of Mn. **(inset)** Normalized emission spectra for three of the samples shows identical spectra for Mn = 0.01 mol% and Mn = 0.1 mol%, but the 0.55 mol% Mn sample exhibits an additional long-wave component, likely due to Mn clusters.

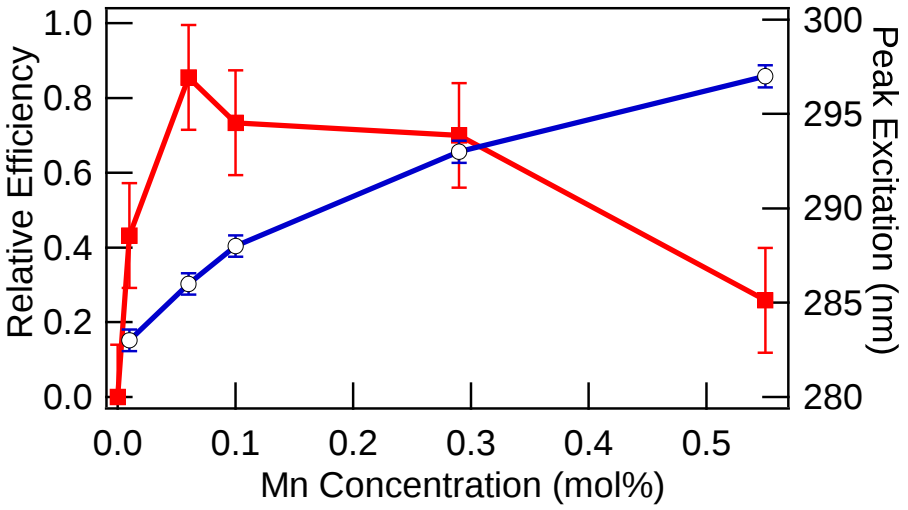

Figure 10. (red square symbols) The relative efficiency of emission under 254 nm excitation as a function of Mn-doping indicates that the 0.01-0.1 mol% range provides best efficiency, with the sample at Mn = 0.06 mol% offering Q.E. of 0.86±0.14. **(blue circle symbols)** The excitation peak shifts to longer wavelength as a function of Mn doping.

The time-resolved decays with 266 nm excitation were acquired and compared as a function of Mn doping in Figure 11. All samples exhibit a 1.25 ms principal decay component. For the three lowest Mn concentration samples (0.01, 0.06 and 0.10 mol%), additional decays correspond to 3-6 ms components, which may be assigned to delayed emission due to the presence of shallow traps at concentrations comparable to the concentration of Mn in those samples. For the two highest concentration samples (0.29 and 0.55 mol%), the Mn concentration may be exceeding its solubility limit for uniform doping into the host, resulting in pairing of Mn dopants, as depicted schematically in Figure 1 [14-16]. For these two samples, faster time components of 0.29-0.35 ms are required to fit the decay curves, indicative of concentration quenching. Fitting parameters are tabulated in Table 2.

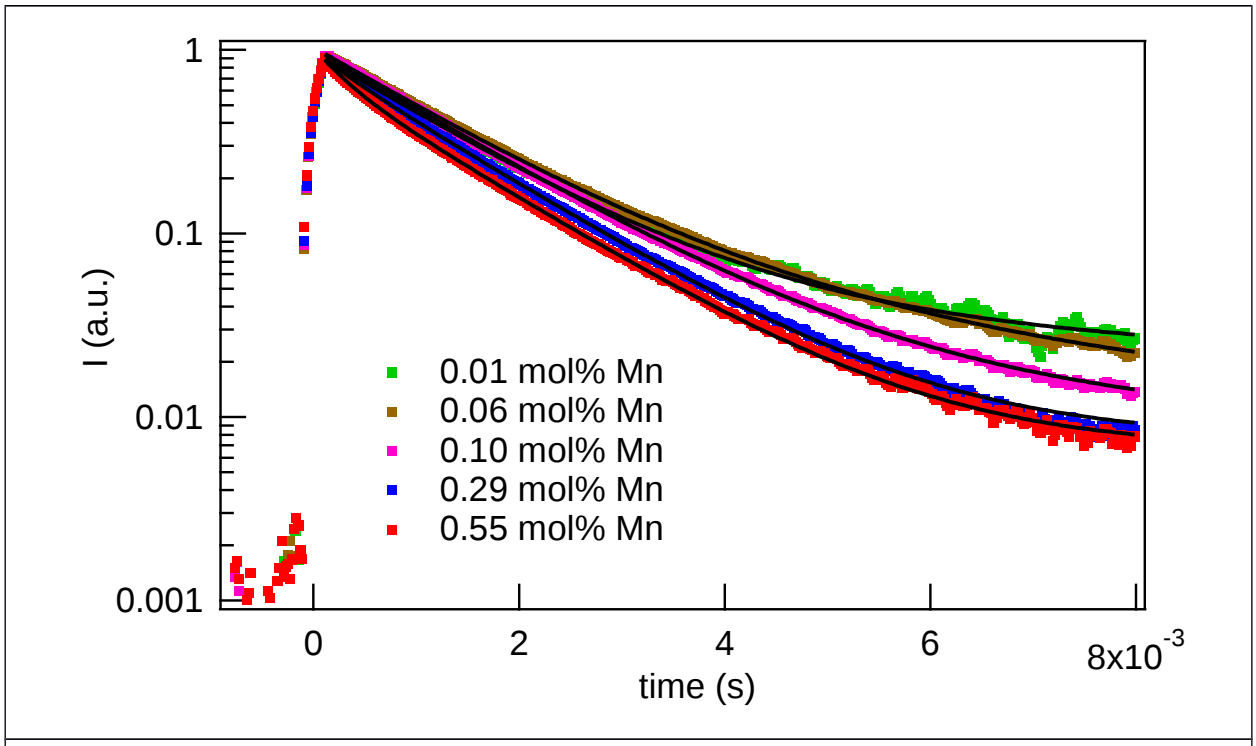

Figure 11. Time-resolved decays of AlN:Mn phosphor samples, acquired with 20 ns, 266 nm pulsed excitation, and with emission detected at 597 nm. All decays are fit to a double exponential with an offset. The principal decay is 1.25 ms and fits are shown as solid black lines.

Table 2. Fitting parameters to decays shown in Figure 11.

Mn. Conc. (at. %)	A_1	τ_1 (ms)	A_2	τ_2 (ms)	offset	Relative LY
0.01	0.87	1.25	0.04	6.30	0.0146	0.43
0.06	0.86	1.25	0.09	4.00	0.0091	0.86
0.10	0.89	1.25	0.04	3.60	0.0077	0.73
0.29	0.79	1.25	0.09	0.35	0.0077	0.70
0.55	0.67	1.25	0.20	0.29	0.0067	0.26

Phosphor stability in Mercury lamp conditions.

There are phosphors, such as $ZnSiO_4$:Mn, that are not stable in the presence of a noble gas/mercury discharge as is used in conventional fluorescent lamps. Whether this instability arises because of chemical, photochemical, plasma-assisted, or other mechanisms is not known, and likely differs among phosphors. To test the chemical compatibility between mercury and AlN:Mn and its stability in fluorescent lamp conditions, a sample of the AlN:Mn phosphor was exposed in the GE proprietary "racetrack" lamp system to the mercury discharge. In the same experiment, a sample of Zn_2SiO_4:Mn was also tested. While the silicate sample darkened quickly (less than 30 minutes), the nitride sample was stable and did not lose any quantum efficiency after a two-hour exposure under the same conditions.

Analysis of tri-phosphor blends.

Proprietary GE models were employed to determine the tradeoffs between lamp efficacy and color rendering index (CRI) when the commercial red-emitting phosphor (Y_2O_3:Eu) is replaced by AlN:Mn in a triphosphor blend. For a blackbody source with color temperature of 4100 K, the standard triphosphor blend yields a lamp efficacy of 92.8 lm/W and CRI of 83. Replacing Y_2O_3:Eu by AlN:Mn increases the lamp efficacy to 93.3 lm/W but decreases CRI to 73. The general principle working here to cause this tradeoff is already illustrated in Figure 2; the Mn emission in AlN is shifted to shorter wavelengths relative to the Eu emission in Y_2O_3.

Conclusions

A series of Mn-doped AlN phosphors were synthesized following a procedure that obtained white powders with high reflectance through the visible wavelengths. The phosphors were characterized via electron microscopy, x-ray diffraction, UV-visible diffuse reflection, excitation and emission spectroscopy, and time-resolved luminescence spectroscopy. The Mn valence in AlN is shown to be divalent, via EXAFS and corroborated by DFT calculations. The highest quantum efficiency AlN:Mn phosphor has 0.06 mol% Mn, and provides a spectrum and integrated intensity comparable to that of Y_2O_3:Eu, with 254 nm excitation. Higher Mn doping leads to concentration quenching and degraded efficiency. The origin of the UV absorption band has been studied via DFT, and is proposed to be due to an aluminum vacancy coupled with oxygen impurity dopants. This site likely associates with Mn^{2+} when synthesized under appropriate conditions, as reported here, resulting in high transfer efficiency from the host to the Mn^{2+} emitter. Excellent survivability of the AlN:Mn phosphor in the mercury lamp conditions has been demonstrated. The AlN:Mn phosphor, in combination with standard green and blue phosphors, provides good color rendering (CRI) and brightness (lm/W) comparable to commercial phosphor blends, suggesting that AlN:Mn could be useful as a replacement for Y_2O_3:Eu in fluorescent lamps.

Acknowledgements

We are grateful to Materion Advanced Chemicals, Milwaukee, WI for the support they provided to our nitride synthesis work. We acknowledge helpful discussions with Lynn Boatner and Michael Chance, of Oak Ridge National Laboratory and Karl Gschneider, Jr. at Ames Laboratory. Funding was provided by the DOE EERE Critical Materials Institute, and work was performed under the auspices of the U. S. Department of Energy by Lawrence Livermore National Laboratory under Contract DE-AC52-07NA27344. The work performed at Ames Laboratory, which is operated for the U.S. DOE by Iowa State University, was under contract # DE-AC02-07CH11358. Release number is LLNL-JRNL- .

References

1. R.-J. Xie, N. Hirosaki, Y. Li and T. Takeda, Materials, 3, 3777-3793 (2010).

2. M. Kubus, K. Levin, S. Kroeker, D. Enseling, T. Jüstel and H.-J. Meyer, Dalton Trans., 2015, 44, 2819 (2015).

3. C.J. Duan, A.C.A. Delsing, H.T. Hintzen, J. Lumin., 129, 645–649 (2009).

4. Z. Zhang, A.C.A. Delsing, P.H.L. Notten, J. Zhao, P. Dorenbos, and H.T. Hintzen, ECS J. Solid State Sci. Tech., 2 (4) R70-R75 (2013).

5. Adams, T.R. AuCoin, G.A. Wolff, J. Electrochem. Soc., 109, 11, 1050-1054 (1962).

6. F.R. Karel, J. Pastrnak, J. Hejduk, V. Losik, Phys. Stat. Sol. 15, 693-699 (1966).

7. Sato, K. Azumada, T. Atsumori, and K. Hara, App. Phys. Lett., 87, 021907 (2005).

8. Sato, K. Azumada, T. Atsumori, K. Hara, J. Crystal Growth 298 379–382 (2007).

9. X.-J. Wang, R.-J. Xie, B. Dierre, T. Takeda, T. Suehiro, N. Hirosaki, T. Sekiguchi, H. Li, Z. Sun, Dalton Trans., (2014).

10. A.M. Srivastava and T.J. Sommerer, Electrochem. Soc. Interface, Summer (1998).

11. M. Ramisetty, S. Sastri, and U. Kashalikar, Am. Ceram. Soc. Bull., 93, 6, 28-31 (2104).

12. S. E. Pratsinis, G. Wang, and S. Panda, T. Guiton and A.W. Weimer, J. Mater. Res., 10, 3, 512-520 (1995).

13. Y. Shimokawa, A. Fujiwara, E. Ionescu, G. Mera, S. Honda, Y. Iwamoto, R. Riedel, J. Ceram. Soc. Japan, 123, 1435, 106-113 (2015).

14. D. S. McClure, J. Chem. Phys. 39, 11, (1963)

15. A.P. Vink, M.A. de Bruin, S. Roke, P.S. Peijzel, and A. Meijerink, J. Electrochem. Soc., 148, 7, E313-E320 (2001).

16. Aoyama, Y. Amano, K. Inoue, S. Honda, S. Hashimoto,Y. Iwamoto, J. Lumin. 136, 411–414 (2013).

17. H. Zhang, M. Zheng, B. Lei, Y. Liu, Y. Xiao, H. Dong, Y. Zhang, and S. Ye, ECS J. Solid State Sci. Tech., 2 (7) R117-R120 (2013).

18. L. Trinkler, B. Berzina, Rad. Measurements, 71, 232-236 (2014).

19. G.A. Slack, L.J. Schowalter, D. Morelli, J.A. Freitas Jr, J. Crystal Growth, 246, 287-298 (2002).

20. R.A. Youngman, J.H. Harris, J. Am. Ceram. Soc., 73, 11, 3238-3246 (1990).

21. E. Polikarpov, D. Catalini, A. Padmaperuma, P. Das, T. Lemmon, B. Arey, C.A. Fernandez, Optical Mat., 46, 614-618 (2015).

22. W. Lehmann, J. Electrochem. Soc. 130, 2, 426-431 (1983).

23. P. E. Blöchl, Phys. Rev. B, 50, 17953 (1994).

24. G. Kresse, J, Hafner, Phys. Rev. B, 47, 558 (1993).

25. G. Kresse, J. Furthmüller, Comput. Mater. Sci., 6, 15 (1996).

26. J. P. Perdew, K. Burke, M. Ernzerhof, Phys. Rev. Lett., 78, 1396 (1997); 78, 1396(E), (1997).

27. J. P. Perdew, M. Ernzerhof, K. Burke, J. Chem. Phys., 105, 9982 (1996).

28. S. B. Zhang, J. E. Northrup, Phys. Rev. Lett., 67, 2339, (1991).

29. Persson, Y.-J. Zhao, S. Lany, A. Zunger, Phys. Rev. B, 72, 035211, (2005).

30. Åberg, P. Erhart, A. J. Williamson, V. Lordi, Phys. Rev. B, 77, 165206, (2008).

31. Makov, M. C. Payne, Phys. Rev. B, 51, 4014 (1995).

32. R. Qiao, T. Chin, T., S.J. Harris, Sh. Yan, W. Yang, Curr. App. Phys., 13, 3 544-8 (2013).

33. Kawai, J., Y. Mizutani, et al. Spectrochimica Acta Part B-Atomic Spectroscopy 55(9): 1385-1395. (2000).

34. M. Benabdesselam, J P. Iacconi, D. Lapraz, P. Grosseau, and B. Guilhot, J. Phys. Chem., 99, 10319-10323 (1995).

35. M.V. Averyanova, I.N. Przhevalskii, S.Yu. Karpov, Yu.N. Makarov, M.S. Ramm, R.A. Talalaev, Mat. Sci. Eng. B43, I67-171 (1997).

36. T. Mattila, R. M. Nieminen, Phys. Rev. B, 54, 16676, (1996).

37. Gorczyca, A. Svane, N. E. Christensen, Phys. Rev. B, 60, 8147, (1999)

38. L. Silvestri, K. Dunn, S. Prawer, F. Ladouceur, Europhys. Lett., 98, 36003, (2012).

39. Q. Yan, A. Janotti, M. Scheffler, C. G. van de Walle, Appl. Phys. Lett., 105, 111104 (2014).

40. Y. Cho, B. Dierre, T. Takeda, K.i Takahashi, N. Hirosaki, and T. Sekiguchi, App. Phys. Express 7, 115503 (2014).

41. Y. Cho, B. Dierre, N. Fukata, N. Hirosaki, K. Marumoto, D. Son, K. Takahashi, T. Takeda, T. Sekiguchi, Scripta Mat., 110, 109–112 (2016).

42. Y. Shi, Y. Wang, Y. Wen, Zh. Zhao, B. Liu and Zh. Yang, Opt. Express, 20, 19, 21656 (2012).

Red-Emitting Manganese-doped Aluminum Nitride Phosphor

Nerine J. Cherepy, Stephen A. Payne, Nicholas M. Harvey, Daniel Åberg, Zachary M. Seeley, Kiel S. Holliday, Ich C. Tran, Fei Zhou, H. Paul Martinez, Jessica M. Demeyer, Alexander D. Drobshoff
Lawrence Livermore National Laboratory, Livermore, CA 94550

Alok M. Srivastava, Samuel J. Camardello, Holly A. Comanzo
GE Global Research, One Research Circle, Niskayuna, NY 12309

Deborah L. Schlagel, Thomas A. Lograsso
Ames Laboratory, Ames, IA 50011

Supplementary Material

Figure X shows XRD spectra before and after nitrogen annealing. There is no evidence of secondary phase in either spectrum, nor of any other significant changes.

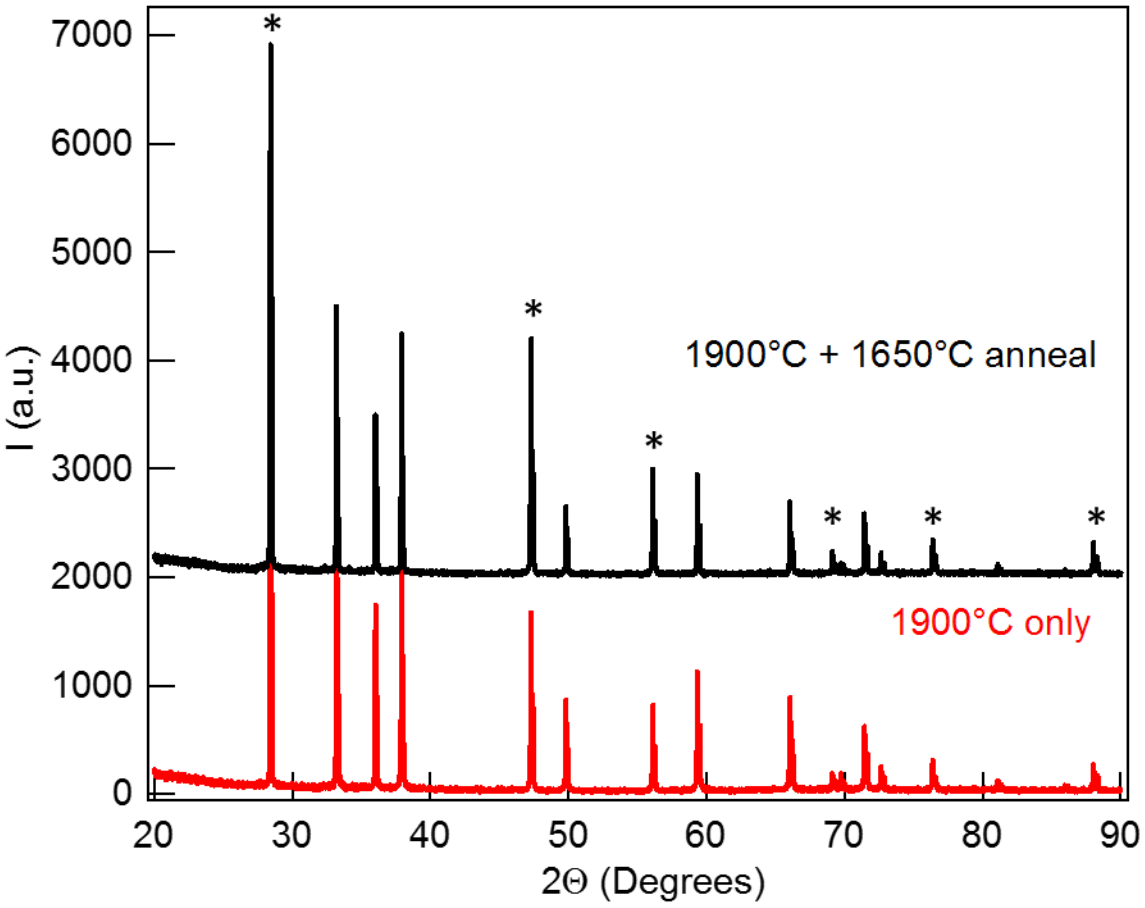

Figure 12. XRD patterns appear unchanged after annealing. Peaks marked with asterisks are due to the Si standard.

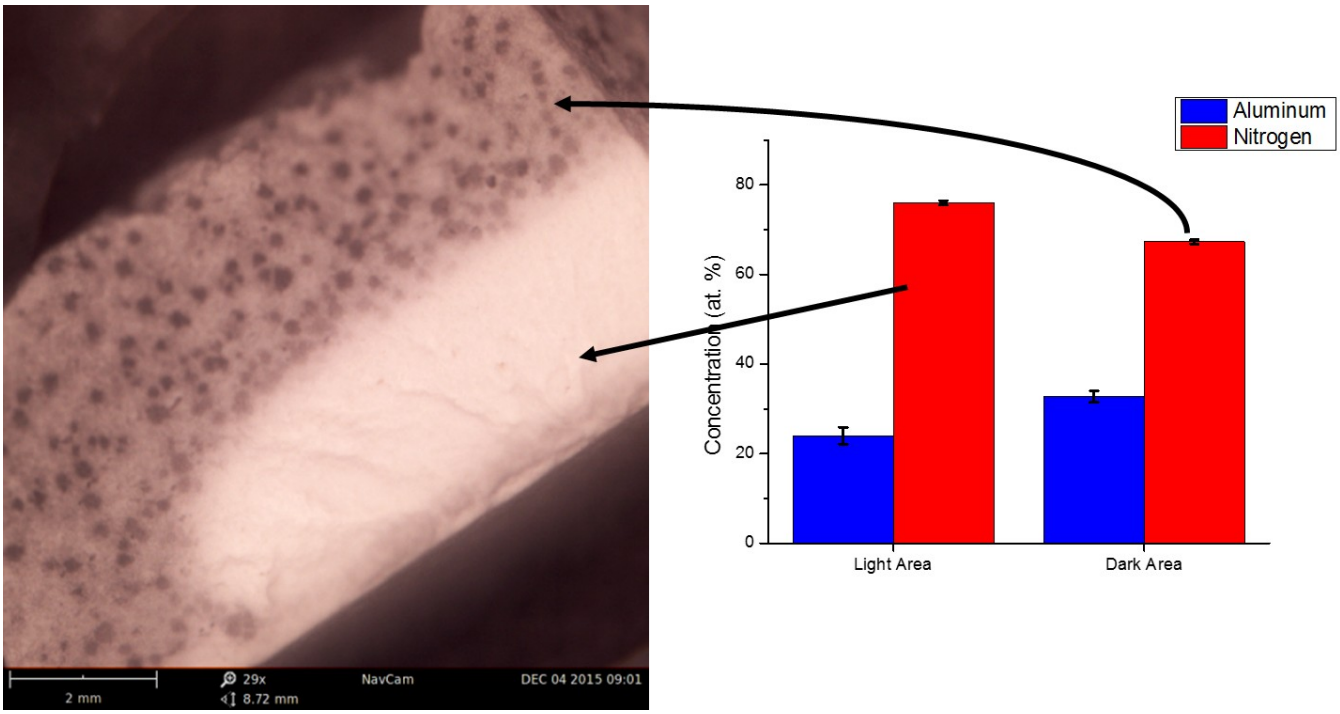

Figure 13. Optical micrograph and EDS spectra of hard-sintered AlN:Mn pellets synthesized at 1900°C and 1500 psi N_2 reveal a correlation between nitrogen deficiency and dark body color of AlN.

Table 3. Effect of Si-doping on effective light yield into the intrinsic (defect-related) broad emission band centered at 400 nm.

% Si	Relative light yield
0	1.00
0.5	1.20
1	1.10
1.5	0.64

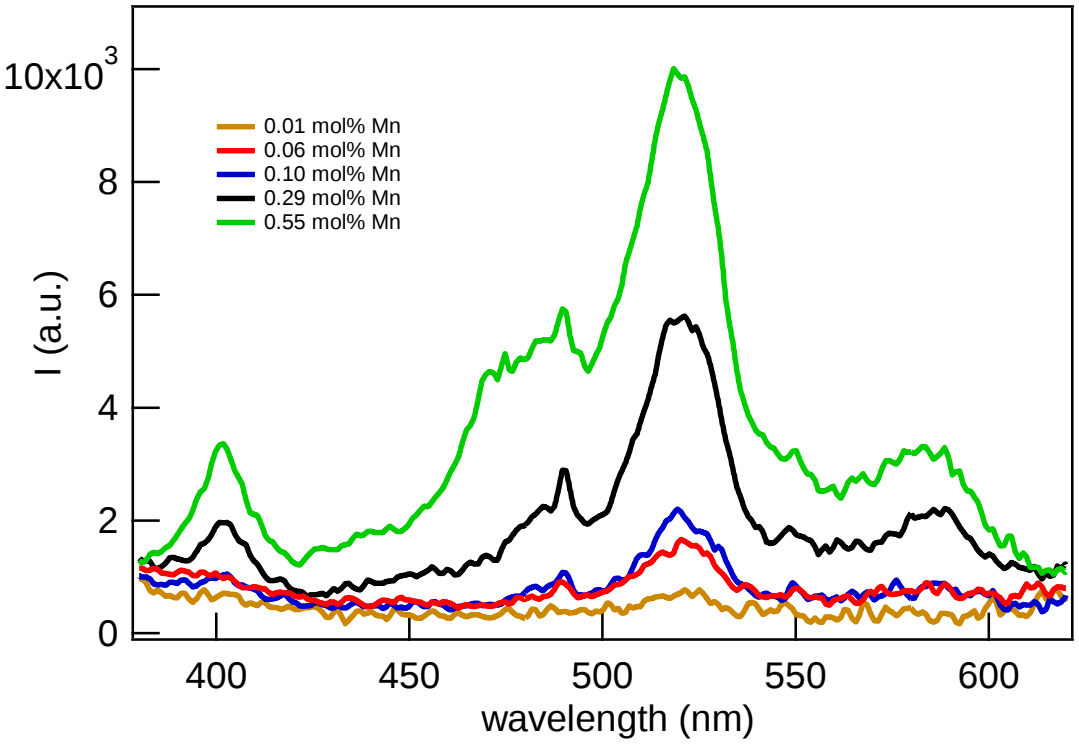

Figure 14. Expanded view of the excitation spectra in the Mn^{2+} absorption region. The peak intensity at 520 nm is found to correlate with the Mn concentration in each sample.